

Article

# Ag<sub>3</sub>PO<sub>4</sub>-TiO<sub>2</sub>-Graphene Oxide Ternary Composites with Efficient Photodegradation, Hydrogen Evolution, and Antibacterial Properties

Fu-Jye Sheu <sup>1</sup>, Chun-Pei Cho <sup>1,\*</sup> , Yu-Ting Liao <sup>2</sup> and Chang-Tze Yu <sup>2</sup>

<sup>1</sup> Department of Applied Materials and Optoelectronic Engineering, National Chi Nan University, Nantou County 54561, Taiwan; s103328503@mail1.ncnu.edu.tw

<sup>2</sup> Department of Applied Chemistry, National Chi Nan University, Nantou County 54561, Taiwan; donuts912@hotmail.com (Y.-T.L.); ctyu@ncnu.edu.tw (C.-T.Y.)

\* Correspondence: cpcho@ncnu.edu.tw

Received: 10 December 2017; Accepted: 29 January 2018; Published: 2 February 2018

**Abstract:** Ag<sub>3</sub>PO<sub>4</sub>-TiO<sub>2</sub>-graphene oxide ternary composite photocatalysts were fabricated by the photocatalytic reduction and ion exchange methods. The properties and photocatalytic activity of the composites were examined, and the photodegradation mechanism was investigated. More TiO<sub>2</sub> nanoparticles in the composites were found to improve light absorption, but caused a larger impedance and inferior charge transport. Excess TiO<sub>2</sub> nanoparticles distributed over the surfaces of Ag<sub>3</sub>PO<sub>4</sub> and graphene oxide decreased the specific surface area and thus lowered light absorbance. An appropriate TiO<sub>2</sub> content enhanced photocatalytic performance. When the molar ratio of Ag<sub>3</sub>PO<sub>4</sub> to TiO<sub>2</sub> was 0.6, the highest efficiency in photodegradation, hydrogen production (with a quantum efficiency of 8.1% and a hydrogen evolution rate of 218.7 μmole·g<sup>-1</sup>·h<sup>-1</sup>) and bacterial inactivation was achieved. Trapping experiments demonstrated that superoxide radicals and holes are the major active species involved in the photodegradation process.

**Keywords:** graphene oxide; titanium dioxide; silver phosphate; photocatalyst; ternary composite; photodegradation; hydrogen evolution; hydrogen production

## 1. Introduction

Since photocatalytic water splitting by titanium dioxide (TiO<sub>2</sub>) was disclosed by Fujishima and Honda in 1972 [1], significant effort has been devoted to highly active photocatalysts, which could have potential applications to hydrogen production from water splitting, water purification and disinfection, and removal and degradation of pollutants [2,3]. Photocatalysis has been considered as an effective, economical, and environmentally-friendly photooxidation process, where the active oxygen-containing radicals produced can remove the contaminants by converting them to non-toxic carbon dioxide (CO<sub>2</sub>), water (H<sub>2</sub>O), etc. [4–7]. The development of new materials to meet the demands for removal and sterilization of the pollutants in water has become urgent. Semiconductor photocatalysts have been widely studied to solve current energy and environmental issues [8–13]. However, the semiconductor materials available to date are generally limited by either poor photocatalytic efficiency in the visible-light range or insufficient charge separation ability [14–17]. In order to address these problems, considerable efforts should be made to the design and fabrication of more effective semiconductors, in order to obtain higher photocatalytic performance.

Recently, Ye et al. have reported that the use of silver orthophosphate (Ag<sub>3</sub>PO<sub>4</sub>) could achieve an extremely high quantum efficiency (QE) of O<sub>2</sub> evolution from water splitting under visible-light irradiation [18]. Since then, Ag<sub>3</sub>PO<sub>4</sub>-based materials have been seen as promising photocatalysts, due to their superior photooxidative capabilities. However, the drawbacks of Ag<sub>3</sub>PO<sub>4</sub>, such as

insolubility in most solvents, instability upon light illumination, and the ease of reduction to weakly active silver (Ag), may greatly restrict its practical applications. To overcome these, diverse approaches have been attempted to promote the stability, usability, and photocatalytic activity of  $\text{Ag}_3\text{PO}_4$ —for example: conjunction with metals giving rise to the surface plasmon resonance (SPR) effect, formation of core-shell nanostructures or complexes with heterostructures [19–26], and combination with graphene or its analogues [24–26]. In particular, the cost could be greatly reduced using graphene oxide (GO) to fabricate the composites containing  $\text{Ag}_3\text{PO}_4$  [26].

Graphene and GO have attracted tremendous attention, due to their large surface areas and high carrier mobility. Various composites based on graphene or GO employed as photocatalysts, to improve the interfacial contact and significantly enhance the photocatalytic activity, have been reported [25,27–35]. Liu et al. reported a GO- $\text{Ag}_3\text{PO}_4$  composite, obtained by an ion exchange method, showing improved antibacterial activity and photodegradation efficiency for organic pollutants [24]. Yang et al. produced a stable graphene- $\text{Ag}_3\text{PO}_4$  composite with good photocatalytic performance by a hydrothermal approach. The size and morphology of  $\text{Ag}_3\text{PO}_4$  particles could be tailored by the electrostatically-driven assembly of silver ions ( $\text{Ag}^+$ ) on the GO surface. Nevertheless, the relatively large size of  $\text{Ag}_3\text{PO}_4$  led to smaller specific surface area, and thus limited photocatalytic activity [26]. Xiang et al. fabricated a nano-sized graphene- $\text{Ag}_3\text{PO}_4$  composite with enhanced visible-light photocatalytic activity for the degradation of methylene blue (MB) by an in-situ growth strategy [36]. They declared that the graphene sheets could provide a greater number of active adsorption sites, suppress charge recombination, and reduce the formation of Ag nanoparticles (NPs).

Compared with the aforementioned binary composites, the ternary system which contains metal oxide,  $\text{Ag}_3\text{PO}_4$ , and graphene or GO has been reported to exhibit even more superior photocatalytic and antibacterial characteristics. Yang et al. prepared the  $\text{TiO}_2$ - $\text{Ag}_3\text{PO}_4$ -graphene ternary composite with improved photocatalytic degradation activity toward organic dye molecules, and enhanced antibacterial activity compared to bare  $\text{Ag}_3\text{PO}_4$ ,  $\text{TiO}_2$ , and binary composites. By adjusting the molar ratio of  $\text{Ag}_3\text{PO}_4$  to  $\text{TiO}_2$  and adding the amount of GO, the photocatalytic and antibacterial activities were regulated [37]. In the next year, the same group reported that the P25- $\text{Ag}_3\text{PO}_4$ -GO ternary composite, with micro-sized  $\text{Ag}_3\text{PO}_4$  and  $\text{TiO}_2$  NPs decorated on the GO sheets, was prepared by electrostatically-driven assembly and an ion exchange method. The efficiency of dye photodegradation and bacterial inactivation could be tuned by varying the amount of GO and the molar ratio of  $\text{Ag}_3\text{PO}_4$  to P25. The dissolved  $\text{Ag}^+$  ions were also considered to play an important role in determining the bactericidal performance [38].

As described above, the effective visible light harvesting, improved separation of photo-excited electron-hole pairs, and fast interfacial charge transfer between different components in a composite are crucial. The intrinsic antibacterial property of  $\text{Ag}_3\text{PO}_4$  is also important. Therefore, what we are more concerned with is the ternary system, and various  $\text{Ag}_3\text{PO}_4$ - $\text{TiO}_2$ -GO (APTGO) ternary composite photocatalysts were obtained by the photocatalytic reduction and ion exchange methods in this study. The presence of  $\text{Ag}_3\text{PO}_4$  and GO has been reported to be beneficial for visible-light absorption [36,38]. Their amounts for fabricating the ternary composites were fixed. Only the amount of  $\text{TiO}_2$  was adjusted to investigate its impact on the photocatalytic performance. The results have demonstrated that an appropriate content of  $\text{TiO}_2$  was indeed contributive to enhanced photocatalytic properties of the APTGO composites. The highest efficiency in photodegradation, hydrogen production from water splitting, and bacterial inactivation was obtained when the molar ratio of  $\text{Ag}_3\text{PO}_4$  to  $\text{TiO}_2$  was 0.6. The photocatalytic mechanism of the APTGO composites was also explored. To the best of our knowledge, this is the first work of accomplishing the application of  $\text{Ag}_3\text{PO}_4$ -based photocatalysts to hydrogen evolution.

## 2. Results and Discussion

XRD patterns are often used to identify the crystal structure of a solid material. The XRD patterns of the APTGO ternary composites are displayed in Figure 1. The diffraction peak at approximately  $25.3^\circ$  is a typical characteristic of  $\text{TiO}_2$  ascribed to anatase (101). The peaks at  $20.9^\circ$ ,  $29.7^\circ$ ,  $33.2^\circ$ ,  $36.6^\circ$ ,  $47.8^\circ$ ,  $52.7^\circ$ ,  $55.0^\circ$ ,  $57.3^\circ$ ,  $61.6^\circ$ ,  $69.8^\circ$ , and  $71.9^\circ$  are attributed to the (110), (200), (210), (211), (310), (222), (320), (321), (400), (420), and (421) planes of  $\text{Ag}_3\text{PO}_4$ , respectively. They demonstrate the presence of  $\text{Ag}_3\text{PO}_4$  in the APTGO composites [37,38]. Nevertheless, there is no characteristic peak of GO observed in Figure 1. Another peak at  $44.3^\circ$  can be indexed to the cubic structure of Ag, corresponding to diffraction from the (200) plane of Ag NPs. Compared to other diffraction peaks, its intensity is relatively small, due to the low Ag contents in the composites [39]. It also indicates traces of zero-valent (neutral) Ag present in the composites, which were produced by the reduction of  $\text{Ag}^+$  ions.

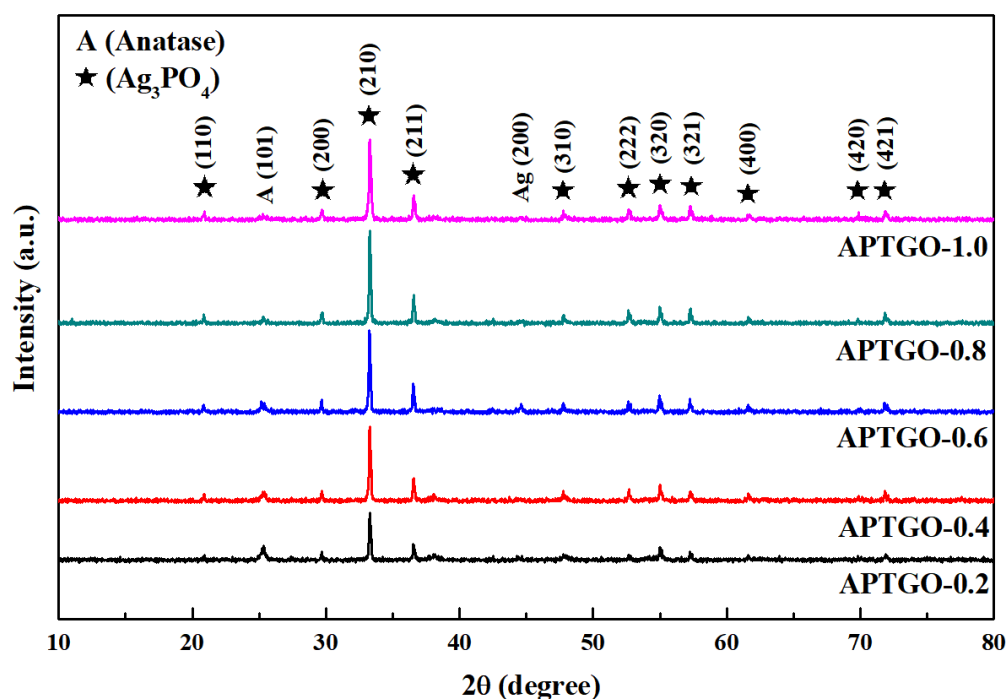


**Figure 1.** XRD patterns of the  $\text{Ag}_3\text{PO}_4$ - $\text{TiO}_2$ -GO (APTGO) ternary composites.

Raman spectroscopy is a widely utilized technique to examine the structures and electronic properties of graphene and its derivatives. Figure 2 shows the Raman spectra of the APTGO ternary composites, ranging from  $100\text{ cm}^{-1}$  to  $2000\text{ cm}^{-1}$ . The five peaks at  $147\text{ cm}^{-1}$ ,  $199\text{ cm}^{-1}$ ,  $399\text{ cm}^{-1}$ ,  $515\text{ cm}^{-1}$ , and  $639\text{ cm}^{-1}$  correspond to the vibrational modes of  $E_g$ ,  $E_g$ ,  $B_{1g}$ ,  $B_{1g}$  and  $E_g$ , of anatase  $\text{TiO}_2$ , respectively [16]. This demonstrates that the  $\text{TiO}_2$  in the five composites is mainly anatase. The two peaks at  $1354\text{ cm}^{-1}$  and  $1594\text{ cm}^{-1}$  are D and G bands, respectively. The D band is due to the presence of disorders in  $\text{sp}^2$ -hybridized carbon systems. It can be used to estimate the defect level and content of impurity in graphene sheets. The G band is derived from the stretching of  $\text{sp}^2$ -hybridized carbon-carbon bonds, and is highly sensitive to strain effects in the  $\text{sp}^2$  system within graphene sheets. Furthermore, the intensity ratio of D and G bands,  $I_D/I_G$ , can be considered as a measure of the relative concentration of local defects or interferences, i.e., to estimate the changes of  $\text{sp}^3$  graphite oxide converting to  $\text{sp}^2$  graphene [40]. Therefore, an increment of  $I_D/I_G$  value implies an increase in the number of defects. From Figure 2, the  $I_D/I_G$  value of GO is calculated to be 1.73. Those for the five composites are in between 1.65 and 1.69, approximate to that of GO. This helps to ascertain the presence of GO in the APTGO composites obtained from the reaction of  $\text{AgNO}_3$  and  $\text{Na}_2\text{HPO}_4$ .

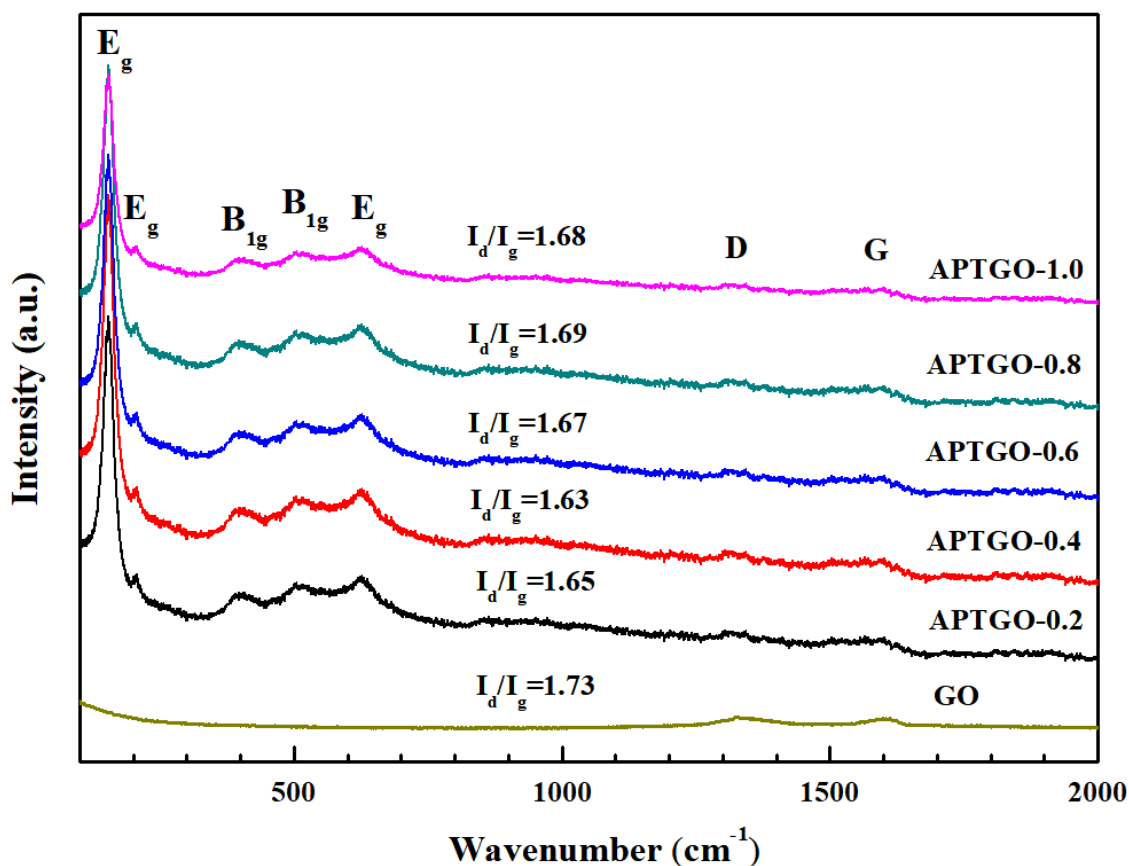
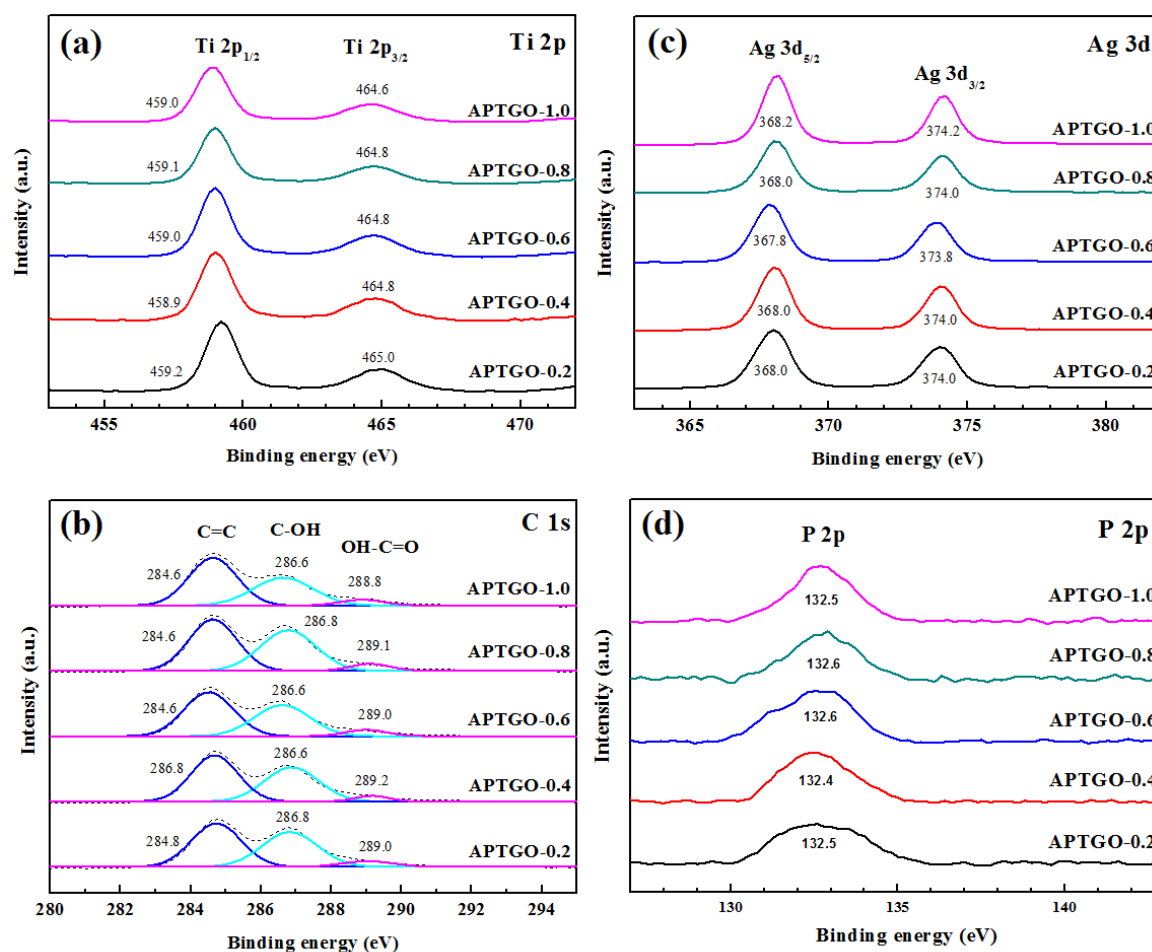


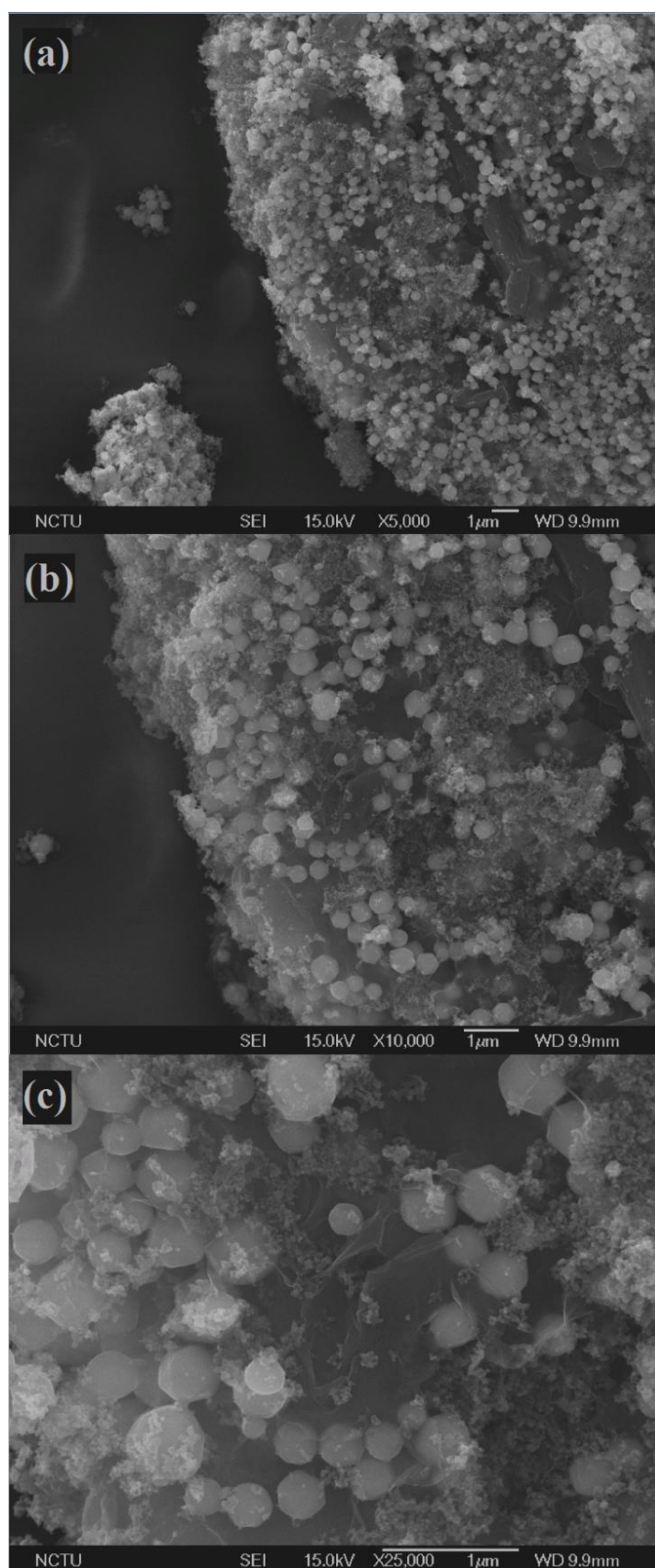
Figure 2. Raman spectra of the APTGO ternary composites.

Figure 3 displays the XPS spectra of the APTGO ternary composites. The compositions of the composites and chemical states of elements can be investigated by XPS. Figure 3a shows the Ti 2p spectra. The two peaks centered at approximately 459.0 eV and 464.7 eV can be ascribed to the Ti 2p<sub>3/2</sub> and Ti 2p<sub>1/2</sub> spin-orbit splitting states, respectively. They are the corresponding feature of Ti-O bonding (Ti<sup>4+</sup>), which is typical for TiO<sub>2</sub>. The difference between the two peaks is 5.7 eV, confirming the existence of O-Ti-O bonds in the composites [41,42]. Figure 3b shows the C 1s spectra. According to the literature, the energy peak centered at approximately 284.6 eV is assigned to sp<sup>2</sup>-hybridized carbon (C=C) atoms, whereas another two weaker peaks with higher binding energies (286 eV to 289 eV) can be assigned to oxygenated carbon atoms such as hydroxyl (C-OH) and carboxyl (HO-C=O) species on the surface [38,43]. In addition, the peaks corresponding to C-OH bonds of the APTGO composites were found to have higher intensity compared to the Ag-TiO<sub>2</sub>-graphene (ATG) ternary composites (already reported elsewhere [44]). This implies that the proportion of GO in the APTGO composites are higher than those in the ATG counterparts, i.e., the extent of GO being reduced to graphene is lower in the APTGO composites. Figure 3c displays the Ag 3d spectra. The two peaks centered at approximately 368.0 eV and 374.0 eV can be attributed to the Ag 3d<sub>5/2</sub> and Ag 3d<sub>3/2</sub> spin-orbit splitting states, respectively. They are assigned to Ag (I), indicating the presence of Ag<sup>+</sup> in the composites [38,45]. Figure 3d displays the P 2p spectra. The peak at approximately 132.5 eV is ascribed to the characteristic of P<sup>5+</sup>, demonstrating the existence of Ag<sub>3</sub>PO<sub>4</sub> in the composites [36,38]. From the XPS results, it is thereby concluded that the preparation of APTGO photocatalysts was successful.



**Figure 3.** X-ray photoelectron spectrometer (XPS) spectra of the APTGO ternary composites: (a) Ti 2p, (b) C 1s, (c) Ag 3d, and (d) P 2p.

The APTGO composites were dispersed on the copper grids with lacey carbon films for SEM observation. Figure 4 shows the surface morphologies of APTGO-0.6 at three different magnifications. Large  $\text{Ag}_3\text{PO}_4$  particles with uneven size distribution and tiny  $\text{TiO}_2$  NPs are deposited on the surface of semitransparent GO [38]. The diameter of the  $\text{Ag}_3\text{PO}_4$  particles is 250 nm to 600 nm approximately. For further confirmation, elemental mappings are examined. Figure 5 reveals the even distribution of the C, O, P, Ti, and Ag elements, and verifies the successful preparation of the APTGO composites again. Figure 6 shows the TEM micrographs of APTGO-0.6. The semitransparent membranous structure of GO can be observed, as shown in Figure 6a,b. A large number of  $\text{TiO}_2$  NPs with a size of around 20 nm to 30 nm, a small amount of Ag NPs, and  $\text{Ag}_3\text{PO}_4$  particles with larger sizes cover the GO sheets. The microstructures of APTGO-0.6 are displayed in Figure 6c,d. The lattice fringe spacing value of 0.34 nm corresponds to the d-spacing of the (101) plane of anatase  $\text{TiO}_2$ . Another two lattice fringe spacing values of 0.20 nm and 0.27 nm correspond to the (200) plane of Ag NPs and the (210) plane of  $\text{Ag}_3\text{PO}_4$  particles, respectively. The TEM results also contribute to confirming the successful preparation of the APTGO ternary composites.



**Figure 4.** SEM micrographs of APTGO-0.6 at the magnifications of (a) 5 K; (b) 10 K; and (c) 25 K.

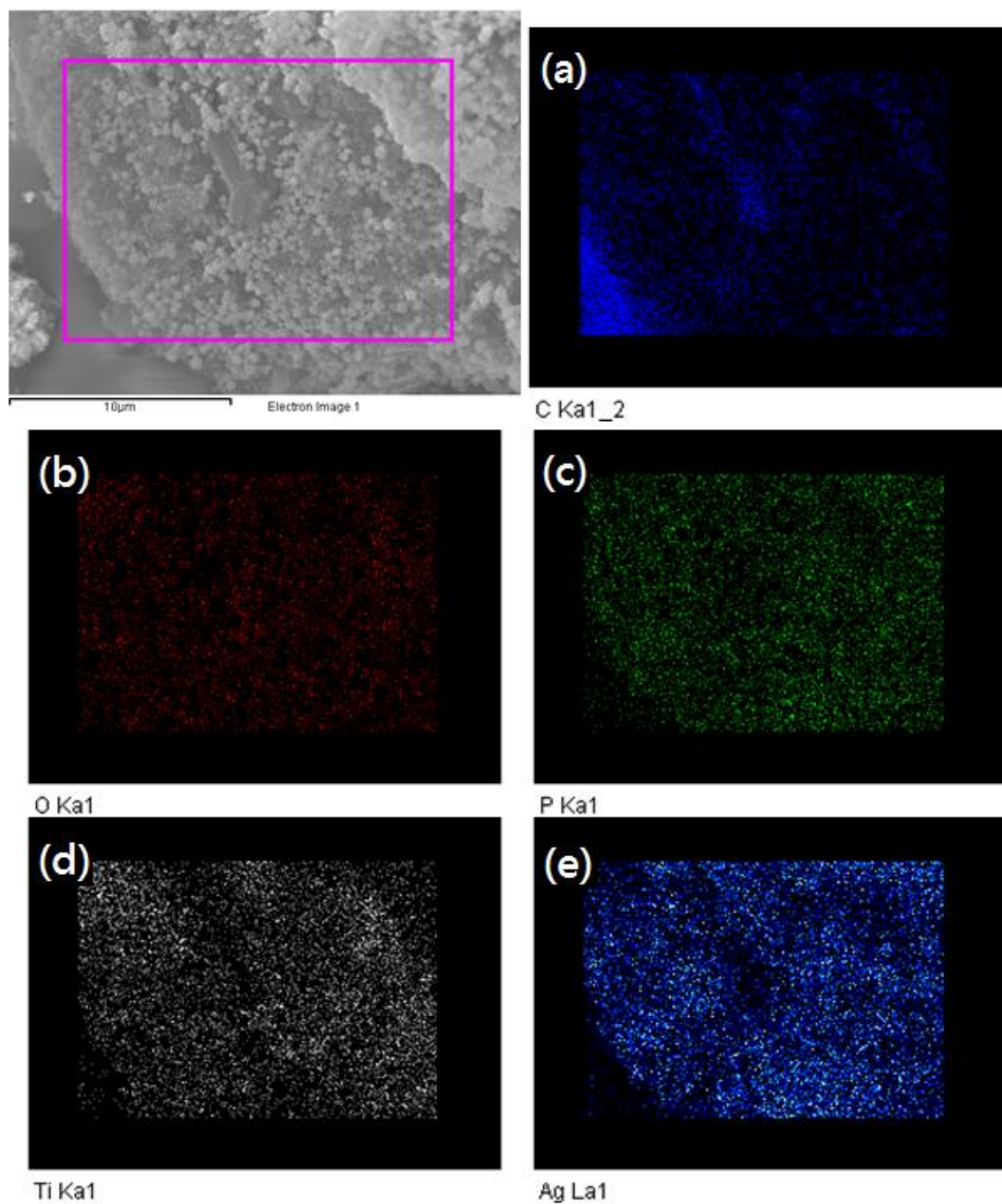


**Figure 5.** Elemental mappings of APTGO-0.6: (a) C, (b) O, (c) P, (d) Ti, and (e) Ag.

Figure 7 displays the UV-Vis absorption spectra of the APTGO ternary composites. According to the literature [36,38], the presence of  $\text{Ag}_3\text{PO}_4$  and GO was reported to be favorable to visible-light absorption. Their amounts employed to fabricate the ternary composites were fixed in this study. Only the amount of  $\text{TiO}_2$  was adjusted, in order to see its impact on photocatalytic performance. As revealed in Figure 7, an increased  $\text{TiO}_2$  content is discovered to improve the visible-light absorbance. However, excess  $\text{TiO}_2$  NPs covering  $\text{Ag}_3\text{PO}_4$  and GO decrease the surface area of a photocatalyst, leading to reduced light harvesting and thereby lower photocatalytic activity. By the plots of the transformed Kubelka-Munk function versus photon energy, the bandgap energy ( $E_g$ ) value for each APTGO ternary composite can be obtained. Among the five composites, APTGO-0.6 exhibits the largest absorbance and the smallest  $E_g$  of 2.61 eV. This implies that the optimum molar ratio of  $\text{Ag}_3\text{PO}_4$  to  $\text{TiO}_2$  in an APTGO photocatalyst is probably 0.6.

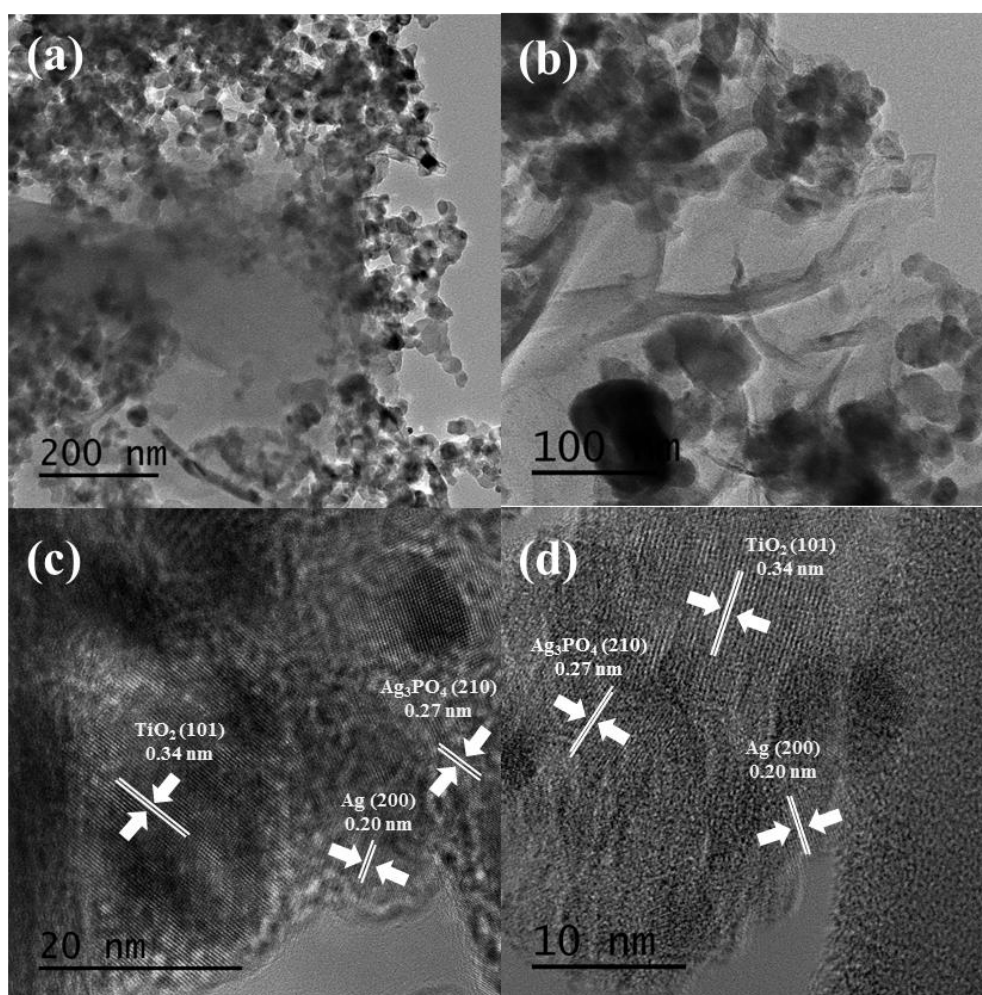


Figure 6. (a,b) TEM images and (c,d) HRTEM microstructures of APTGO-0.6.

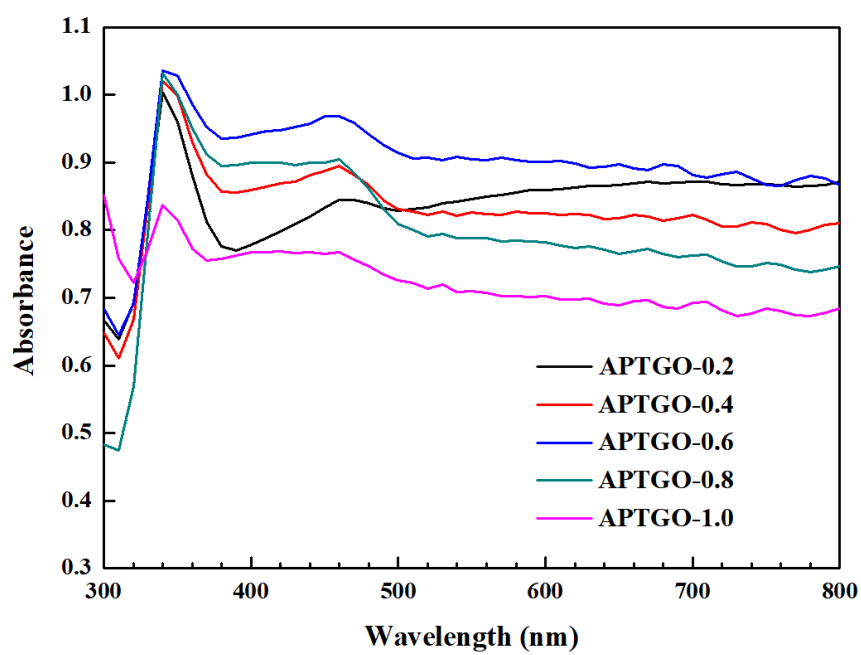


Figure 7. UV-Vis absorption spectra of the APTGO ternary composites.

The oxidation and reduction capabilities of a material can be evaluated by the magnitude of oxidation and reduction potentials obtained by CV tests. Figure 8a shows the CV curves of the electrodes covered with the APTGO photocatalysts. Among the five composites, APTGO-1.0 exhibits the largest oxidation potential, implying that it is the strongest oxidizer and acquires electrons most readily. This can explain why it also shows the largest oxidation current. Figure 8b displays the Nyquist plots of the electrodes covered with the APTGO composites obtained by EIS analysis. The plot for APTGO-1.0 shows the smallest semicircle, which implies the smallest interfacial impedance. The electrochemical results have revealed the best conductivity and the most efficient charge transport ability of APTGO-1.0. An increased content of  $\text{TiO}_2$  is found to cause a reduced oxidation current and a larger interfacial impedance, and inferior charge transport is thus resulted. Since the amounts of  $\text{Ag}_3\text{PO}_4$  and GO used in the preparation processes for every composite are fixed, it can be consequently deduced that excess  $\text{TiO}_2$  is unfavorable to the photocatalytic activity of an APTGO composite. Because the electrochemical experiments were not performed under light irradiation, the results of CV and EIS are not necessarily consistent with those of photocatalysis and antibacterial tests. Namely, the photocatalyst (APTGO-1.0) having the largest oxidation current on the CV curve does not necessarily show the highest photocatalytic activity. Since APTGO-0.6 exhibits the largest absorbance as shown in Figure 7, it is then speculated that an appropriate content of  $\text{TiO}_2$  is required to achieve the optimum photocatalytic performance for an APTGO ternary composite.

The decolorization of dye is often utilized to evaluate the photocatalytic capacity of a photocatalyst. Figure 9 displays the photodegradation curves of MO by the APTGO composites, in which  $C_0$  and  $C$  represent the MO concentrations before and after the xenon lamp irradiation, respectively. Among the five ternary composites, APTGO-0.6 exhibits the highest performance. It makes 80% of dye degraded when the duration for irradiation is 120 min, demonstrating the superior photodegradation efficiency of APTGO-0.6. According to first-order kinetics, its reaction rate constant ( $k'$ ) is calculated to be 0.0083, which is the largest among the five photocatalysts. By contrast, APTGO-0.2 and APTGO-1.0 show the lowest photodegradation efficiency. Their  $k'$  is around 0.0027, which is merely one third of that of APTGO-0.6. Since APTGO-0.6 exhibits the best optical response and photodegradation efficiency, it can be concluded that an appropriate  $\text{TiO}_2$  content in an APTGO photocatalyst is certainly conducive to enhanced photocatalytic performance, and the most appropriate molar ratio of  $\text{Ag}_3\text{PO}_4$  to  $\text{TiO}_2$  is 0.6.

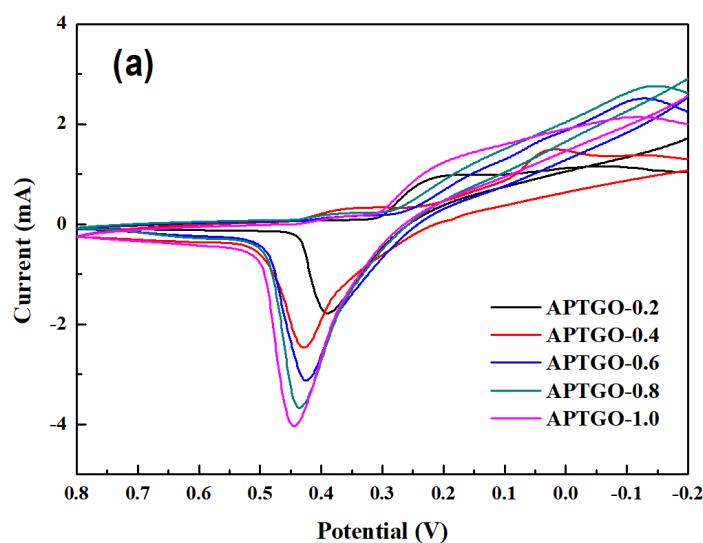
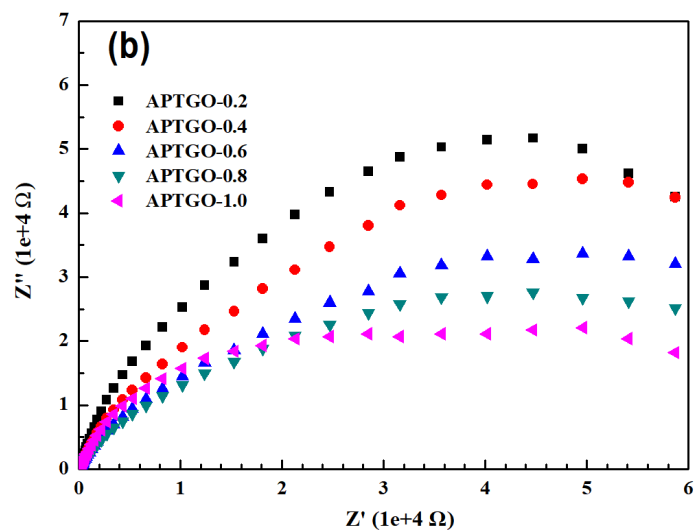
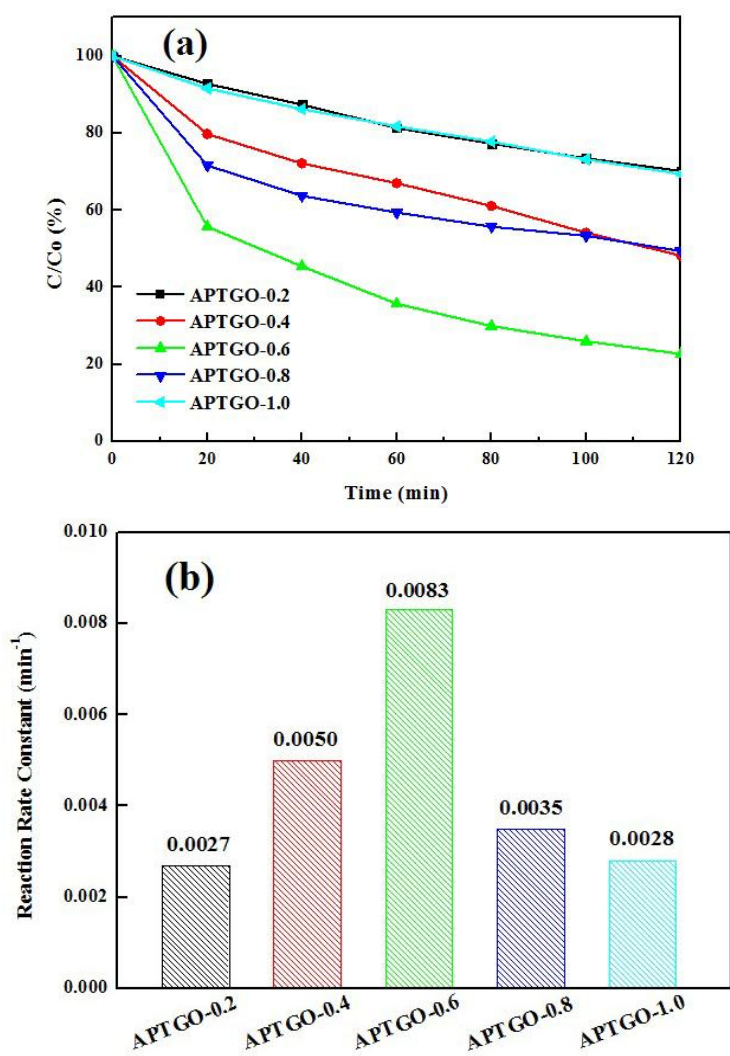


Figure 8. Cont.



**Figure 8.** (a) CV curves and (b) Nyquist plots of the electrodes covered with the APTGO ternary composites.



**Figure 9.** (a) Photodegradation curves and (b) corresponding reaction rate constants of the APTGO ternary composites.

To explore the main active species involved in the photodegradation process of the APTGO composites, hole and radical trapping experiments were carried out, and the photocatalytic reaction mechanism was thereby elucidated. Three scavengers, each with a concentration of 2 mM, were selected for the trapping experiments [38,46]. Benzoquinone (BQ), ammonium oxalate (AO) and *tert*-butyl alcohol (TBA) were used for capturing superoxide radicals ( $O_2^{\bullet-}$ ), holes ( $h^+$ ), and hydroxyl radicals ( $OH^{\bullet}$ ), respectively. As shown in Figure 10a, the degradation efficiency for APTGO-0.6 is 98.6% when no scavenger is used after two hours of irradiation. The inactivation of the photocatalyst with the degradation efficiency of 19.8% and 16.3% was remarkably caused by BQ and AO, respectively. On the other hand, there is not much reduction in the degradation efficiency when TBA is used. The results have demonstrated that the irradiated  $O_2^{\bullet-}$  and photo-induced  $h^+$  play important roles and contribute the most to the APTGO photocatalytic system.  $OH^{\bullet}$  is considered to be of lesser importance, since TBA is less involved in photodegradation process [36,38].

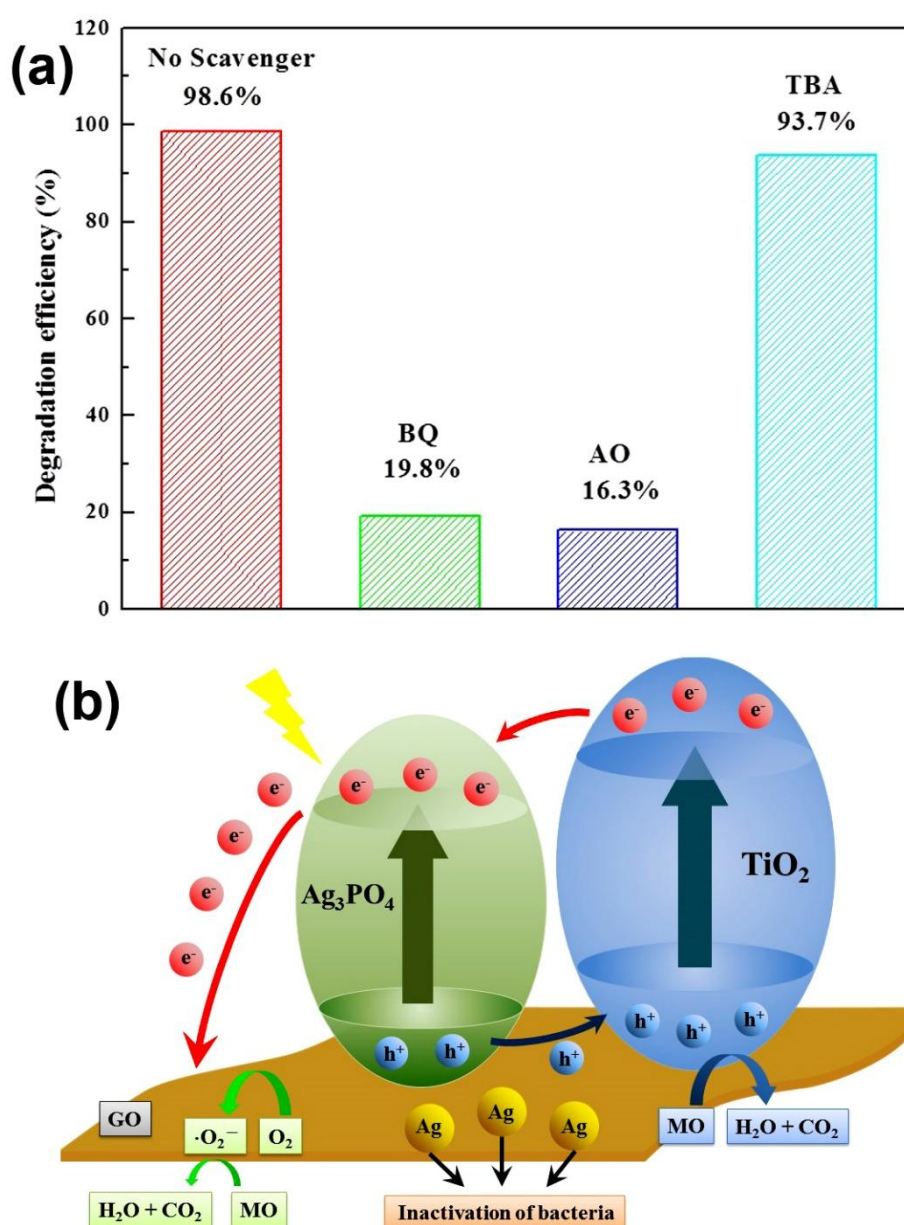


**Figure 10.** (a) Hole and radical trapping experiments using APTGO-0.6; (b) Schematic photocatalytic mechanism of the APTGO ternary composites.

All the APTGO ternary composites prepared in this study are of powder type, stored at the room temperature in a dry box. According to the literature [26,36,38,47], the composites containing  $\text{Ag}_3\text{PO}_4$  have the problem of poor optical stability only when they are put in water, where the  $\text{Ag}^+$  ion is easily reduced to metallic-state Ag under light irradiation. Therefore, the APTGO composites are considered to be stable by our way of storage. Based on the aforementioned results and by referring to the literature, a probable photocatalytic mechanism of the APTGO composites can be proposed, as depicted in Figure 10b. Under the solar simulator light irradiation, both  $\text{TiO}_2$  and  $\text{Ag}_3\text{PO}_4$  are excited to generate electron-hole pairs. The electrons in the CB of  $\text{TiO}_2$  are transferred to the CB of  $\text{Ag}_3\text{PO}_4$ , and then migrated rapidly to the surface of GO. When the electrons are away from  $\text{Ag}_3\text{PO}_4$ , the probability of  $\text{Ag}^+$  ions being reduced to metallic-state Ag is decreased. This is conducive to improving the optical stability of  $\text{Ag}_3\text{PO}_4$ . Meanwhile, the high surface area of GO is beneficial to the adsorptions of dye and bacteria, which are decomposed by  $\text{O}_2\bullet^-$  produced from  $\text{O}_2$  molecules captured on the GO surface. On the other hand, the holes in the VB of  $\text{Ag}_3\text{PO}_4$  are transferred to the VB of  $\text{TiO}_2$ , to make dye and bacteria oxidized. This photocatalytic mechanism is established by the synergistic effect of  $\text{Ag}_3\text{PO}_4$ ,  $\text{TiO}_2$  and GO.

Figure 11a displays the hydrogen evolution curves of the APTGO composites. A methanol solution was employed as the sacrificial agent. As predicted, the results of hydrogen evolution are found to have a similar trend to those of photodegradation. A higher hydrogen evolution rate can be obtained when an appropriate content of  $\text{TiO}_2$  is used to fabricate a composite. After six hours of photocatalytic water splitting, the photocatalyst exhibiting the maximum hydrogen production amount ( $1312 \mu\text{mole}\cdot\text{g}^{-1}$ ) is APTGO-0.6. Compared to APTGO-1.0 showing the smallest amount of hydrogen production ( $362 \mu\text{mole}\cdot\text{g}^{-1}$ ), there is an over three-fold difference in the amount of hydrogen production. This again demonstrates that the most appropriate molar ratio of  $\text{Ag}_3\text{PO}_4$  to  $\text{TiO}_2$  is 0.6. Figure 11b displays the mass-normalized evolution rates and QE of the APTGO composites. According to the literature [48,49], QE can be calculated after obtaining the mass-normalized evolution rate by:

$$\begin{aligned} \text{QE}(\%) &= \frac{\text{number of reacted electrons}}{\text{number of incident photons}} \times 100 \\ &= \frac{\text{number of evolved H}_2\text{ molecules} \times 2}{\text{number of incident photons}} \times 100 \end{aligned}$$

The QE and mass-normalized hydrogen evolution rate for APTGO-0.6 are 8.1% and  $218.7 \mu\text{mole}\cdot\text{g}^{-1}\cdot\text{h}^{-1}$ , respectively. Nevertheless, those for APTGO-1.0 are 2.2% and  $60.4 \mu\text{mole}\cdot\text{g}^{-1}\cdot\text{h}^{-1}$ , respectively. The difference of QE between the two photocatalysts is 5.9%. The results have illustrated that when an APTGO composite has fixed contents of  $\text{Ag}_3\text{PO}_4$  and GO for hydrogen production from water splitting, the optimum  $\text{TiO}_2$  content should be present in order to achieve the highest photocatalytic efficiency.

The antibacterial tests were all designed with a controlled trial. Due to the different absorbance at 600 nm when a different APTGO photocatalyst was used, the OD 600 value at the very beginning for every test was treated as 1.00. The relation charts of bacterial growth rate versus time can be then achieved, as displayed in Figure 12. The antibacterial effects by an excess amount (1.0 mg) of the photocatalysts are found to be too good, so that the difference in bacterial growth rate can hardly be distinguished, as revealed in Figure 12a. The bacterial growth rate for every test group is around 1.0. There is no obvious trend. Moreover, the OD 600 values were observed to be lower than 0.50 after bacterial culture for 200 min. By contrast, the OD 600 value for the control group without using any photocatalyst increased to 2.85 after bacterial culture for 400 min. The growth rate of *E. coli* for the control group was 22.6. These indicate that the APTGO composites can effectively inhibit the growth of *E. coli*. To be able to distinguish the difference in bacterial growth rate, a smaller amount of the photocatalysts (0.3 mg) was used for the antibacterial tests. As shown in Figure 12b, a reduced amount of the photocatalysts can slow down the bacterial growth, and the difference in bacterial growth rate can be differentiated more readily. It is revealed that APTGO-0.6 exhibits the

highest antibacterial activity, demonstrating the excellent antibacterial effect of the APTGO ternary composite photocatalysts.

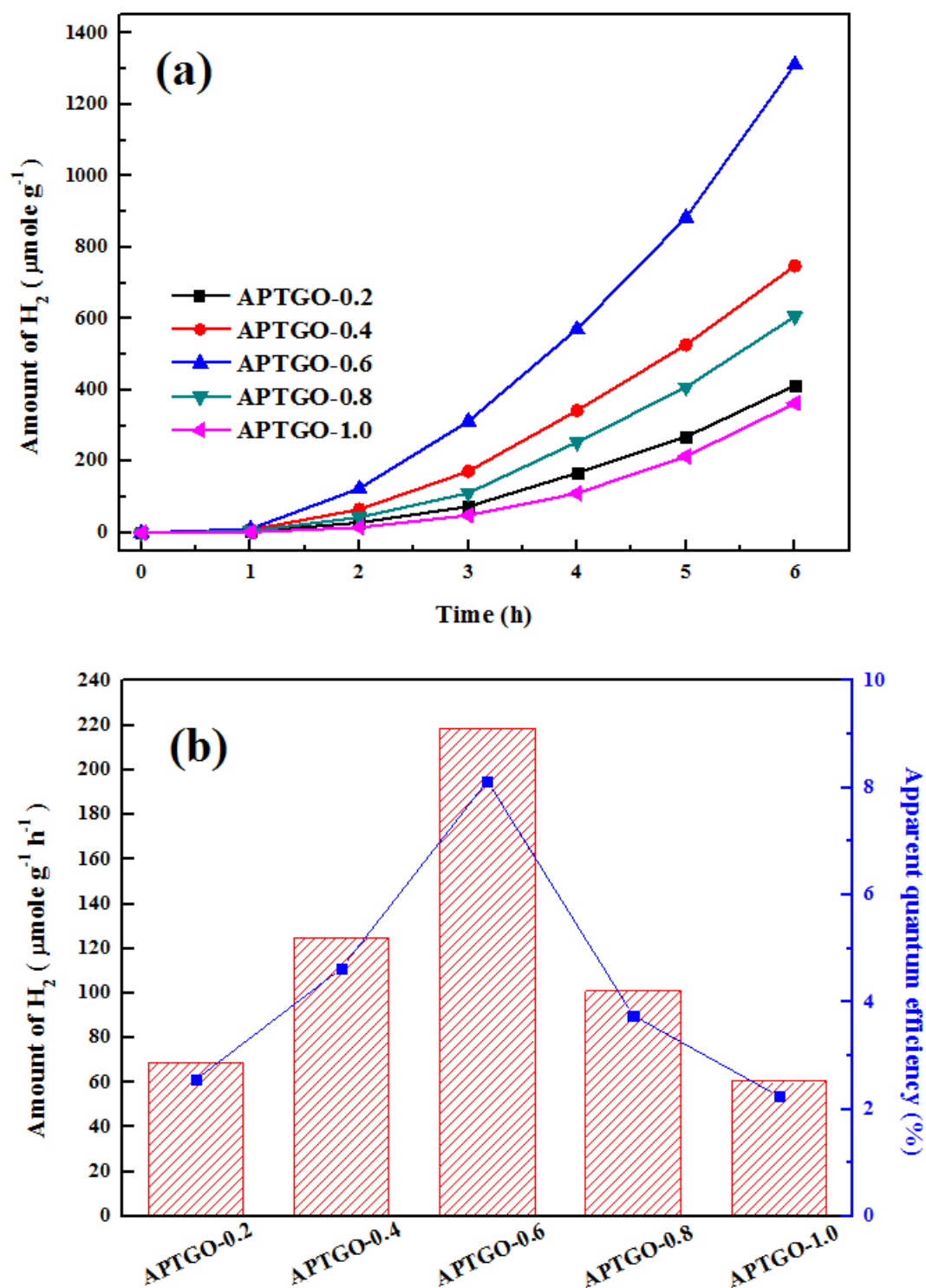
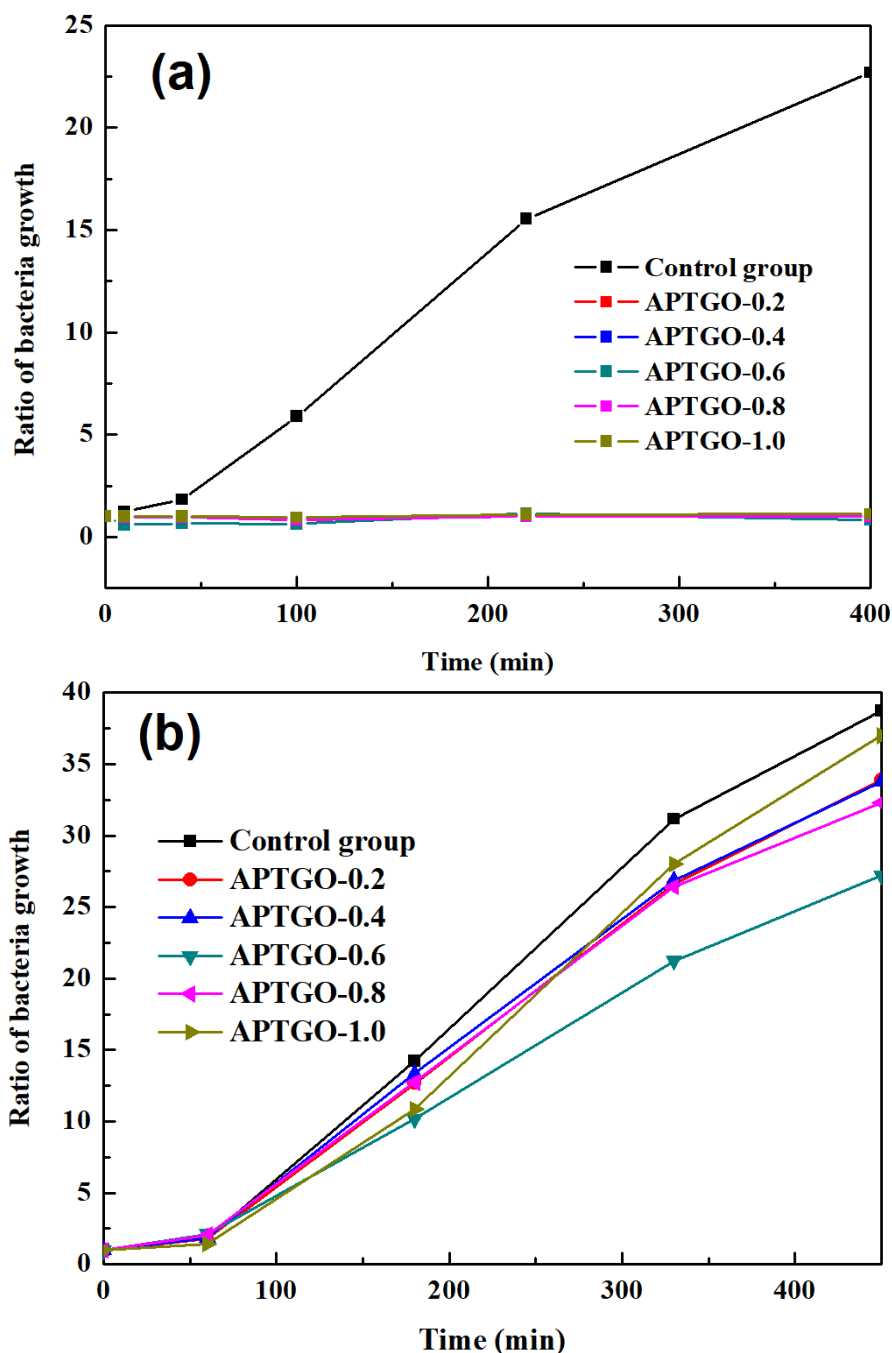


Figure 11. (a) Hydrogen evolution curves; (b) mass-normalized evolution rates and quantum efficiency (QE) of the APTGO ternary composites.



**Figure 12.** Relation charts of bacterial growth rate versus time when the amount of APTGO photocatalysts used is (a) 1.0 mg and (b) 0.3 mg.

### 3. Experimental

#### 3.1. Preparation of Graphene Oxide

GO was synthesized from graphite powder (UniRegion Bio-Tech, Hsinchu, Taiwan) by the modified Hummers' method [50]. A graphite oxidation procedure was carried out before the synthesis of GO [41,51]. A total of 4 g of graphite powder was added into a solution composed of 2 g of potassium persulfate ( $K_2S_2O_8$ ) (J. T. Baker, Phillipsburg, NJ, USA), 2 g of phosphorus pentoxide ( $P_2O_5$ ) (J. T. Baker, Phillipsburg, NJ, USA), and 30 mL of conc. sulfuric acid ( $H_2SO_4$ ). The mixture solution was heated to 80 °C under a continuous stirring for 6 h. When it was cooled down to the room temperature,

rinse with deionized (DI) water was performed repeatedly by centrifugation until the neutral pH level was achieved. Afterwards, 4 g of the pre-oxidized graphite powder was added into 100 mL of conc.  $\text{H}_2\text{SO}_4$  solution in an ice bath. Then, 12 g of potassium permanganate ( $\text{KMnO}_4$ ) (J. T. Baker, Phillipsburg, NJ, USA) was slowly added at 35 °C. The stirring was continued for 2 h until the color of the mixture turned to dark brown. Subsequently, a solution containing 200 mL of DI water and 40 mL of hydrogen peroxide ( $\text{H}_2\text{O}_2$ , 30 wt. % in water) (Sigma-Aldrich, St. Louis, MO, USA) was added slowly as a violent chemical reaction occurred. The color turned to yellow brown when the reaction was completed. The obtained product was put in a dilute aqueous solution of hydrochloric acid (HCl) so as to remove metal ions. After ultrasonication for 1 h, rinse with DI water was repeatedly performed by centrifugation until the neutral pH level was achieved to obtain GO powder.

### 3.2. Fabrication of $\text{Ag}_3\text{PO}_4$ - $\text{TiO}_2$ -GO Ternary Composites

20 mg of GO was added into 100 mL of DI water to prepare the GO solution. Ultrasonication was performed for 2 h to better disperse GO. 153 mg of silver nitrate ( $\text{AgNO}_3$ ) was dissolved in 100 mL of DI water to prepare the 9 mM  $\text{AgNO}_3$  solution. Afterwards, the GO and  $\text{AgNO}_3$  solutions were mixed to form a mixture of  $\text{Ag}^+$ /GO, which was stirred overnight. Various weights (24 mg, 30 mg, 40 mg, 60 mg, and 120 mg) of P25 were added in 100 mL of DI water to prepare the  $\text{TiO}_2$  solutions with various concentrations (3 mM, 3.75 mM, 5 mM, 7.5 mM, and 15 mM, respectively). After stirring for 30 min, the  $\text{TiO}_2$  solutions were added into the  $\text{Ag}^+$ /GO mixture and then stirred for another 30 min to form a  $\text{TiO}_2$ / $\text{Ag}^+$ /GO mixture solution. Subsequently, the 3 mM sodium phosphate ( $\text{Na}_2\text{HPO}_4$ ) solution was added dropwise till the yellow brown precipitate appeared. Rinses by DI water and absolute ethanol were repeated several times, followed by centrifugation to collect the APTGO ternary composites, which were then dried at 60 °C for 24 h. These composites were named APTGO-z, in which z represented the molar ratio of  $\text{Ag}_3\text{PO}_4$  to  $\text{TiO}_2$  during the preparation processes. There were five ratios ( $z = 0.2, 0.4, 0.6, 0.8, \text{ and } 1.0$ ) for comparison.

### 3.3. Photocatalysis

The photodegradation of methylene orange (MO) was carried out, to evaluate the photocatalytic activity of the photocatalysts. A total of 200 mg of an APTGO composite was dispersed in 200 mL of MO solution with a concentration of 20 ppm. The 350 W xenon lamp placed 15 cm above the reactor was used as a solar simulator light source. Prior to irradiation, the mixture was kept in the dark, stirring for 20 min so as to establish an adsorption-desorption equilibrium. Under irradiation, 8 mL aliquots from each sample were taken out at the desired time intervals, followed by centrifugation and filtration to remove the photocatalyst. The supernatant was used to determine the concentration of residual dye in the solution, analyzed by recording the characteristic optical absorbance using a UV-Vis spectrophotometer. Another reactor with a volume of 65 mL was used for hydrogen production from water splitting. A 300 W xenon lamp was employed as its solar simulator light source. The fixed distance between the reactor and lamp was 14 cm. At first, 20 mg of an APTGO composite was dispersed in methanol (20 vol. % in water) in the reactor. Prior to irradiation, the mixture solution was degassed for 20 min by high nitrogen gas. A strong stir was kept for six hours during the irradiation. The gas generated in the reactor was collected once per hour. It went through a thin stainless steel pipeline and was injected into a gas chromatograph. Then the amount of hydrogen produced from water splitting could be recorded.

### 3.4. Antibacterial Test

Lysogeny broth with the concentration of 20 mg/L was used as the nutritionally rich medium. *Escherichia coli* (*E. coli*) was added to the nutrient broth and cultivated in a rotary shaker at room temperature for 12 h, until the stationary growth phase was reached. Further dilution to the required density was performed, to prepare the bacteria solution for antibacterial tests. Amounts of 0.3 mg and 1.0 mg of each composite were mixed with 20 mL of the bacteria solution in glass tubes, respectively.

At the desired times (10 min, 40 min, 100 min, 220 min, and 400 min), 1 mL aliquots from each tube were taken out, followed by centrifugation to remove the composite and acquire the supernatant. The absorbance at 600 nm (OD 600) of each supernatant was recorded. The antibacterial properties of the composites were then compared by the plot of OD 600 versus time.

### 3.5. Characterizations

The surface morphologies of the APTGO ternary composites were examined by a field emission gun scanning electron microscope (SEM) (Hitachi, Tokyo, Japan). The microstructures and lattice fringes were observed by a high-resolution transmission electron microscope (HRTEM) (JEOL, Tokyo, Japan). The elemental mappings were obtained by the energy-dispersive X-ray spectroscopy (EDX). The X-ray diffraction (XRD) patterns (Shimadzu, Kyoto, Japan), ranging from  $10^\circ$  to  $80^\circ$  ( $2\theta$ ), were collected by an X-ray powder diffractometer with copper  $K_\alpha$  radiation ( $\lambda = 1.5406 \text{ \AA}$ ). The absorption spectra, ranging from 300 nm to 800 nm, were recorded by the UV-Vis spectrophotometer (Hitachi, Tokyo, Japan). The chemical compositions of the composites were examined by the X-ray photoelectron spectrometer (XPS) (Ulvac-Phi, Kanagawa, Japan). According to the binding energies of photoelectrons emitted from the surface of a composite, the chemical states of elements could be ascertained. The vibrational modes of molecules were identified, and the chemical structures of composites were thus determined by Raman spectroscopy. A three-electrode configuration was utilized for the electrochemical measurements, including cyclic voltammetry (CV) and electrochemical impedance spectroscopy (EIS), by a potentiostat/galvanostat analyzer (CH Instruments, Austin, TX, USA), using a 0.5 M sodium sulfate ( $\text{Na}_2\text{SO}_4$ ) solution as the electrolyte. The composite powder was mixed with anhydrous ethanol to form a paste, which was coated on the FTO conductive glass by a doctor blade method to form the working electrode. A silver chloride ( $\text{Ag}/\text{AgCl}$ ) electrode and a platinum (Pt) wire served as the reference and auxiliary electrodes, respectively. The scanning rate for CV was  $0.05 \text{ V}\cdot\text{s}^{-1}$ . The frequency range for EIS was  $10^{-2} \text{ Hz}$  to  $10^5 \text{ Hz}$ . The AC amplitude was set as 10 mV between two electrodes.

## 4. Conclusions

The APTGO ternary composites were fabricated by the photocatalytic reduction and ion exchange methods, and applied as photocatalysts. The presence of  $\text{Ag}_3\text{PO}_4$  and GO in the composites was verified by XRD, Raman, and XPS spectra. The deposition and distribution of  $\text{TiO}_2$  NPs and  $\text{Ag}_3\text{PO}_4$  particles on the GO sheets were examined by SEM and TEM. The results of absorption spectra, electrochemical analysis, photodegradation, and hydrogen evolution demonstrated that an appropriate content of  $\text{TiO}_2$  was certainly contributive to enhanced photocatalytic properties of the APTGO composites. Excess  $\text{TiO}_2$  NPs covering  $\text{Ag}_3\text{PO}_4$  particles and GO sheets were found to decrease the specific surface area of a photocatalyst, leading to lower light absorbance and inferior charge transfer. The optimum molar ratio of  $\text{Ag}_3\text{PO}_4$  to  $\text{TiO}_2$  was evidenced to be 0.6, with which APTGO-0.6 showed the highest efficiency in photodegradation, hydrogen production, and bacterial inactivation. The highest QE and mass-normalized hydrogen evolution rate were 8.1% and  $218.7 \mu\text{mole}\cdot\text{g}^{-1}\cdot\text{h}^{-1}$ , respectively. By holes and radicals trapping experiments, the photocatalytic mechanism of the APTGO composites could be proposed. It has been verified that  $\text{O}_2\bullet^-$  and  $\text{h}^+$  are the major active species involved in the photodegradation process.

**Acknowledgments:** Supports from the Ministry of Science and Technology Taiwan and National Chi Nan University are gratefully appreciated.

**Author Contributions:** Chun-Pei Cho conceived and designed the experiments; Fu-Jye Sheu performed the experiments; Chun-Pei Cho supervised Fu-Jye Sheu to analyze the data; Yu-Ting Liao and Chang-Tze Yu helped Fu-Jye Sheu to carry out the antibacterial tests; Chun-Pei Cho wrote the paper.

**Conflicts of Interest:** The authors declare no conflict of interest. The founding sponsors had no role in the design of the study; in the collection, analyses, or interpretation of data; in the writing of the manuscript, and in the decision to publish the results.

## References

1. Fujishima, A.; Honda, K. Electrochemical photolysis of water at a semiconductor electrode. *Nature* **1972**, *238*, 37–38. [[CrossRef](#)] [[PubMed](#)]
2. Kubacka, A.; Fernandez-Garcia, M.; Colon, G. Advanced nanoarchitectures for solar photocatalytic applications. *Chem. Rev.* **2012**, *112*, 1555–1614. [[CrossRef](#)] [[PubMed](#)]
3. Tong, H.; Ouyang, S.X.; Bi, Y.P.; Umezawa, N.; Oshikiri, M.; Ye, J.H. Nano-photocatalytic materials: Possibilities and challenges. *Adv. Mater.* **2012**, *24*, 229–251. [[CrossRef](#)] [[PubMed](#)]
4. Wang, J.L.; Xu, L.J. Advanced oxidation processes for wastewater treatment: Formation of hydroxyl radical and application. *Crit. Rev. Environ. Sci. Technol.* **2012**, *42*, 251–325. [[CrossRef](#)]
5. Sin, J.C.; Lam, S.M.; Mohamed, A.R.; Lee, K.T. Degrading endocrine disrupting chemicals from wastewater by photocatalysis: A review. *Int. J. Photoenergy* **2012**, *2012*. [[CrossRef](#)]
6. Silva, C.P.; Otero, M.; Esteves, V. Processes for the elimination of estrogenic steroid hormones from water: A review. *Environ. Pollut.* **2012**, *165*, 38–58. [[CrossRef](#)] [[PubMed](#)]
7. Limburg, B.; Bouwman, E.; Bonnet, S. Molecular water oxidation catalysts based on transition metals and their decomposition pathways. *Coord. Chem. Rev.* **2012**, *256*, 1451–1467. [[CrossRef](#)]
8. Fox, M.A.; Dulay, M.T. Heterogeneous photocatalysis. *Chem. Rev.* **1993**, *93*, 341–357. [[CrossRef](#)]
9. Tang, J.; Zou, Z.; Ye, J. Efficient photocatalytic decomposition of organic contaminants over  $\text{CaBi}_2\text{O}_4$  under visible-light irradiation. *Angew. Chem. Int. Ed.* **2004**, *43*, 4463–4466. [[CrossRef](#)] [[PubMed](#)]
10. Yao, W.; Huang, C.; Ye, J. Hydrogen production and characterization of  $\text{MLaSrNb}_2\text{NiO}_9$  (M = Na, Cs, H) based photocatalysts. *Chem. Mater.* **2010**, *22*, 1107–1113. [[CrossRef](#)]
11. Maeda, K.; Teramura, K.; Lu, D.; Saito, N.; Inoue, Y.; Domen, K. Noble-metal/ $\text{Cr}_2\text{O}_3$  core/shell nanoparticles as a cocatalyst for photocatalytic overall water splitting. *Angew. Chem. Int. Ed.* **2006**, *45*, 7806–7809. [[CrossRef](#)] [[PubMed](#)]
12. Wang, S.; Yi, L.; Halpert, J.; Lai, X.; Liu, Y.; Cao, H.; Yu, R.; Wang, D.; Li, Y. A novel and highly efficient photocatalyst based on P25-graphdiyne nanocomposite. *Small* **2012**, *8*, 265–271. [[CrossRef](#)] [[PubMed](#)]
13. Du, J.; Lai, X.; Yang, N.; Zhai, J.; Kisailus, D.; Su, F.; Wang, D.; Jiang, L. Hierarchically ordered macro-mesoporous  $\text{TiO}_2$ -graphene composite films: Improved mass transfer, reduced charge recombination, and their enhanced photocatalytic activities. *ACS Nano* **2011**, *5*, 590–596. [[CrossRef](#)] [[PubMed](#)]
14. Tian, G.; Fu, H.; Jing, L.; Xin, B.; Pan, K. Preparation and characterization of stable biphasic  $\text{TiO}_2$  photocatalyst with high crystallinity, large surface area, and enhanced photoactivity. *J. Phys. Chem. C* **2008**, *112*, 3083–3089. [[CrossRef](#)]
15. Lai, Y.; Meng, M.; Yu, Y.; Wang, X.; Ding, T. Photoluminescence and photocatalysis of the flower-like nano-ZnO photocatalysts prepared by a facile hydrothermal method with or without ultrasonic assistance. *Appl. Catal. B* **2011**, *105*, 335–345. [[CrossRef](#)]
16. Ingram, D.; Linic, S. Water splitting on composite plasmonic-metal/semiconductor photoelectrodes: Evidence for selective plasmon-induced formation of charge carriers near the semiconductor surface. *J. Am. Chem. Soc.* **2011**, *133*, 5202–5205. [[CrossRef](#)] [[PubMed](#)]
17. Wang, P.; Huang, B.B.; Qin, X.Y.; Zhang, X.Y.; Dai, Y.; Wei, J.Y.; Whangbo, M.H.  $\text{Ag@AgCl}$ : A highly efficient and stable photocatalyst active under visible light. *Angew. Chem. Int. Ed.* **2008**, *47*, 7931–7933. [[CrossRef](#)] [[PubMed](#)]
18. Yi, Z.G.; Ye, J.H.; Kikugawa, N.; Kako, T.; Ouyang, S.X.; Stuart-Williams, H.; Yang, H.; Cao, J.Y.; Luo, W.J.; Li, Z.S.; et al. An orthophosphate semiconductor with photooxidation properties under visible-light irradiation. *Nat. Mater.* **2010**, *9*, 559–564. [[CrossRef](#)] [[PubMed](#)]
19. Bi, Y.P.; Hu, H.Y.; Ouyang, S.X.; Jiao, Z.B.; Lu, G.X.; Ye, J.H. Selective growth of metallic Ag nanocrystals on  $\text{Ag}_3\text{PO}_4$  submicro-cubes for photocatalytic applications. *Chem. Eur. J.* **2012**, *18*, 14272–14275. [[CrossRef](#)] [[PubMed](#)]
20. Bi, Y.P.; Hu, H.Y.; Ouyang, S.X.; Jiao, Z.B.; Lu, G.X.; Ye, J.H. Selective growth of  $\text{Ag}_3\text{PO}_4$  submicro-cubes on Ag nanowires to fabricate necklace-like heterostructures for photocatalytic applications. *J. Mater. Chem.* **2012**, *22*, 14847–14850. [[CrossRef](#)]
21. Dinh, C.T.; Nguyen, T.D.; Kleitz, F.; Do, T.O. Large-scale synthesis of uniform silver orthophosphate colloidal nanocrystals exhibiting high visible light photocatalytic activity. *Chem. Commun.* **2011**, *47*, 7797–7799. [[CrossRef](#)] [[PubMed](#)]

22. Rawal, S.B.; Sung, S.D.; Lee, W.I. Novel Ag<sub>3</sub>PO<sub>4</sub>/TiO<sub>2</sub> composites for efficient decomposition of gaseous 2-propanol under visible-light irradiation. *Catal. Commun.* **2012**, *17*, 131–135. [[CrossRef](#)]
23. Khan, A.; Qamar, M.; Muneer, M. Synthesis of highly active visible-light-driven colloidal silver orthophosphate. *Chem. Phys. Lett.* **2012**, *519*, 54–58. [[CrossRef](#)]
24. Liu, L.; Liu, J.C.; Sun, D.D. Graphene oxide enwrapped Ag<sub>3</sub>PO<sub>4</sub> composite: Towards a highly efficient and stable visible-light-induced photocatalyst for water purification. *Catal. Sci. Technol.* **2012**, *2*, 2525–2532. [[CrossRef](#)]
25. Liu, Y.P.; Fang, L.; Lu, H.D.; Li, Y.W.; Hu, C.Z.; Yu, H.G. One-pot pyridine-assisted synthesis of visible-light-driven photocatalyst Ag/Ag<sub>3</sub>PO<sub>4</sub>. *Appl. Catal. B Environ.* **2012**, *115*, 245–252. [[CrossRef](#)]
26. Yang, X.F.; Cui, H.Y.; Li, Y.; Qin, J.L.; Zhang, R.X.; Tang, H. Fabrication of Ag<sub>3</sub>PO<sub>4</sub>-graphene composites with highly efficient and stable visible light photocatalytic performance. *ACS Catal.* **2013**, *3*, 363–369. [[CrossRef](#)]
27. Xiang, Q.J.; Yu, J.G.; Jaroniec, M. Graphene-based semiconductor photocatalysts. *Chem. Soc. Rev.* **2012**, *41*, 782–796. [[CrossRef](#)] [[PubMed](#)]
28. Xiang, Q.J.; Yu, J.G.; Jaroniec, M. Synergetic effect of MoS<sub>2</sub> and graphene as cocatalysts for enhanced photocatalytic H<sub>2</sub> production activity of TiO<sub>2</sub> nanoparticles. *J. Am. Chem. Soc.* **2012**, *134*, 6575–6578. [[CrossRef](#)] [[PubMed](#)]
29. Xiang, Q.J.; Yu, J.G.; Jaroniec, M. Enhanced photocatalytic H<sub>2</sub>-production activity of graphene-modified titania nanosheets. *Nanoscale* **2011**, *3*, 3670–3678. [[CrossRef](#)] [[PubMed](#)]
30. Li, Q.; Guo, B.D.; Yu, J.G.; Ran, J.R.; Zhang, B.H.; Yan, H.J.; Gong, J.R. Highly efficient visible-light-driven photocatalytic hydrogen production of CdS-cluster-decorated graphene nanosheets. *J. Am. Chem. Soc.* **2011**, *133*, 10878–10884. [[CrossRef](#)] [[PubMed](#)]
31. Akhavan, O. Graphene nanomesh by ZnO nanorod photocatalysts. *ACS Nano* **2010**, *4*, 4174–4180. [[CrossRef](#)] [[PubMed](#)]
32. Zhu, M.S.; Chen, P.L.; Liu, M.H. Graphene oxide enwrapped Ag/AgX (X = Br, Cl) nanocomposite as a highly efficient visible-light plasmonic photocatalyst. *ACS Nano* **2011**, *5*, 4529–4536. [[CrossRef](#)] [[PubMed](#)]
33. Zeng, P.; Zhang, Q.; Peng, T.; Zhang, X. One-pot synthesis of reduced graphene oxide-cadmium sulfide nanocomposite and its photocatalytic hydrogen production. *Phys. Chem. Chem. Phys.* **2011**, *13*, 21496–21502. [[CrossRef](#)] [[PubMed](#)]
34. Peng, T.; Li, K.; Zeng, P.; Zhang, Q.; Zhang, X. Enhanced photocatalytic hydrogen production over graphene oxide-cadmium sulfide nanocomposite under visible light irradiation. *J. Phys. Chem. C* **2012**, *116*, 22720–22726. [[CrossRef](#)]
35. Jia, T.; Kolpin, A.; Ma, C.; Chan, R.C.T.; Kwok, W.M.; Tsang, S.C.E. A graphene dispersed CdS-MoS<sub>2</sub> nanocrystal ensemble for cooperative photocatalytic hydrogen production from water. *Chem. Commun.* **2014**, *50*, 1185–1188. [[CrossRef](#)] [[PubMed](#)]
36. Xiang, Q.; Lang, D.; Shen, T.; Liu, F. Graphene-modified nanosized Ag<sub>3</sub>PO<sub>4</sub> photocatalysts for enhanced visible-light photocatalytic activity and stability. *Appl. Catal. B* **2015**, *162*, 196–203. [[CrossRef](#)]
37. Yang, X.; Qin, J.; Jiang, Y.; Li, R.; Li, Y.; Tang, H. Bifunctional TiO<sub>2</sub>/Ag<sub>3</sub>PO<sub>4</sub>/ graphene composites with superior visible light photocatalytic performance and synergistic inactivation of bacteria. *RSC Adv.* **2014**, *4*, 18627–18636. [[CrossRef](#)]
38. Yang, X.; Qin, J.; Jiang, Y.; Chen, K.; Yan, X.; Zhang, D.; Li, R.; Tang, H. Fabrication of P25/Ag<sub>3</sub>PO<sub>4</sub>/graphene oxide heterostructures for enhanced solar photocatalytic degradation of organic pollutants and bacteria. *Appl. Catal. B* **2015**, *166*, 231–240. [[CrossRef](#)]
39. Xu, T.; Zhang, L.; Cheng, H.; Zhu, Y. Significantly enhanced photocatalytic performance of ZnO via graphene hybridization and the mechanism study. *Appl. Catal. B Environ.* **2011**, *101*, 382–387. [[CrossRef](#)]
40. Zhang, Y.; Zhang, N.; Tang, Z.R.; Xu, Y.J. Improving the photocatalytic performance of graphene-TiO<sub>2</sub> nanocomposites via a combined strategy of decreasing defects of graphene and increasing interfacial contact. *Phys. Chem. Chem. Phys.* **2012**, *14*, 9167–9175. [[CrossRef](#)] [[PubMed](#)]
41. Wen, Y.; Ding, H.; Shan, Y. Preparation and visible light photocatalytic activity of Ag/TiO<sub>2</sub>/graphene nanocomposite. *Nanoscale* **2011**, *3*, 4411–4417. [[CrossRef](#)] [[PubMed](#)]
42. McCafferty, E.; Wightman, J.P. Determination of the concentration of surface hydroxyl groups on metal oxide films by a quantitative XPS method. *Surf. Interface Anal.* **1998**, *26*, 549–564. [[CrossRef](#)]
43. Yumitori, S. Correlation of C1s chemical state intensities with the O1s intensity in the XPS analysis of anodically oxidized glass-like carbon samples. *J. Mater. Sci.* **2000**, *35*, 139–146. [[CrossRef](#)]

44. Sheu, F.J.; Cho, C.P. Investigation of the appropriate content of graphene in Ag-TiO<sub>2</sub>-graphene ternary nanocomposites applied as photocatalysts. *Int. J. Hydrogen Energy* **2017**, *42*, 17020–17029. [[CrossRef](#)]
45. Hu, X.; Zhu, Q.; Wang, X.; Kawazoe, N.; Yang, Y. Nonmetal-metal-semiconductor-promoted P/Ag/Ag<sub>2</sub>O/Ag<sub>3</sub>PO<sub>4</sub>/TiO<sub>2</sub> photocatalyst with superior photocatalytic activity and stability. *J. Mater. Chem. A* **2015**, *3*, 17858–17865. [[CrossRef](#)]
46. Yang, M.Q.; Zhang, N.; Xu, Y.J. Synthesis of fullerene-, carbon nanotube-, and graphene-TiO<sub>2</sub> nanocomposite photocatalysts for selective oxidation: A comparative study. *ACS Appl. Mater.* **2013**, *5*, 1156–1164. [[CrossRef](#)] [[PubMed](#)]
47. Chai, B.; Li, J.; Xu, Q. Reduced graphene oxide grafted Ag<sub>3</sub>PO<sub>4</sub> composites with efficient photocatalytic activity under visible-light irradiation. *Ind. Eng. Chem. Res.* **2014**, *53*, 8744–8752. [[CrossRef](#)]
48. Phan, T.D.N.; Luo, S.; Liu, Z.; Gamalski, A.D.; Tao, J.; Xu, W.; Stach, E.A.; Polyansky, D.E.; Senanayake, S.D.; Fujita, E.; et al. Striving toward noble-metal-free photocatalytic water splitting: The hydrogenated-graphene-TiO<sub>2</sub> prototype. *Chem. Mater.* **2015**, *27*, 6282–6296. [[CrossRef](#)]
49. Braslavsky, S.E.; Braun, A.M.; Cassano, A.E.; Emeline, A.V.; Litter, M.I.; Palmisano, L.; Parmon, V.N.; Serpone, N. Glossary of terms used in photocatalysis and radiation catalysis. *Pure Appl. Chem.* **2011**, *83*, 931–1014. [[CrossRef](#)]
50. Hummers, W.S.; Offeman, R.E. Preparation of graphitic oxide. *J. Am. Chem. Soc.* **1958**, *80*, 1339. [[CrossRef](#)]
51. Kovtyukhova, N.I.; Ollivier, P.J.; Martin, B.R.; Mallouk, T.E.; Chizhik, S.A.; Buzaneva, E.V.; Gorchinskiy, A.D. Layer-by-layer assembly of ultrathin composite films from micron-sized graphite oxide sheets and polycations. *Chem. Mater.* **1999**, *11*, 771–778. [[CrossRef](#)]



© 2018 by the authors. Licensee MDPI, Basel, Switzerland. This article is an open access article distributed under the terms and conditions of the Creative Commons Attribution (CC BY) license (<http://creativecommons.org/licenses/by/4.0/>).